Australasian Physical & Engineering Sciences in Medicine (2019) 42:53–63
https://doi.org/10.1007/s13246-018-0711-2

SCIENTIFIC PAPER

Multiband ultra-thin flexible on-body transceivers for wearable health informatics

Mubasher Ali[1] · Junaid Zafar[1] · Haroon Zafar[2,3] · Martin O'Halloran[3,4] · Faisal Sharif[2,3,4,5,6]

Received: 29 December 2017 / Accepted: 8 November 2018 / Published online: 15 November 2018

Abstract

Substantial concentration has been associated to the monitoring of vital signs and human activity using wireless body area networks. However, one of the key technical challenges is to characterize an optimized transceiver geometry for desired isolation/bandwidth and specific absorption rate (SAR) characteristics, independent of transceiver chip on-body location. A microwave performance evaluation of monopole wearable transceiver was completed and results presented. A novel on-body antenna transceiver was designed, simulated and fabricated using an ultra-thin substrate RO 3010 (h = 250 µm) that ensures compactness and enhanced flexibility. The designed transceiver was evolved using very high value of dielectric constant using CST® Studio Suit and FEKO® numerical platforms. The on-body characterization for both fatty and bone tissues was experimentally verified for a bandwidth of 200 MHz. The fabricated configuration and real-time testing provides very promising microwave radiation parameters with a gain of 2.69 dBi, $S_{11} < -13$ dB at an operational frequency of 2.46 GHz. Multi-banding was achieved by introducing fractals in the design of the printed monopole. SAR calculations for feet, head and arm at microwave power levels ranging from 100 to 800 mW are incorporated. Furthermore, the real time data acquisition using developed transceiver and its experimental verification is illustrated.

Keywords Wearable biomedical transceiver · Specific absorption rate (SAR) · Fractals · Printed monopole · Health informatics · Cloud computing

Introduction

The availability of innovative electronics in combination with internet of things (IoT) has opened up new avenues of research in the realm of wearable and implantable health care devices [1]. Wearable devices support non-invasive vital signs monitoring on a real time basis to establish an individual's health baseline and can alert medical professionals of any anomalies [2]. To precisely quantify clinical parameters in an unobtrusive manner and manage chronic diseases in elderly patients and those with special disabilities, wearable devices are crucial [3–5]. Wearable medical devices using wireless body area network (WBAN), interconnects sensors in, on and around the body to provide radio coverage of about 10 m [6]. On the signal-processing front, there is a need to develop machine-learning decision models to process heterogeneous data to characterize individual patient behaviour and to complete a reliable risk assessment. WBAN suffer from adoption and implementation challenges that include: sensor sensitivity issues [7], energy efficiency [8, 9], on-chip processing and multiplexing [10, 11], quality of service [12], transmission scheduling [13], privacy protection and security issues [14, 15]. This paper characterizes an effective transceiver for wearable health informatics coupled to external base station devices for relaying patient data onwards for post-processing. Existing efforts in this area

✉ Junaid Zafar
chairperson.engineering@gcu.edu.pk

1 Department of Electrical Engineering, Faculty of Engineering, Government College University, Lahore, Pakistan

2 Cardiovascular Research Centre, School of Medicine, National University of Ireland Galway, Galway, Ireland

3 Lambe Institute for Translational Research, National University of Ireland Galway, Galway, Ireland

4 Translational Medical Devices Lab, University Hospital Galway, Galway, Ireland

5 CÚRAM, SFI Centre for Research in Medical Devices, Galway, Ireland

6 BioInnovate Ireland, Galway, Ireland

include micro-strip antennas [17], slot antennas [19], patch antennas [16], printed antennas [18], reconfigurable antennas [20] and antennas based on meta-materials [21], textile antennas [22] UWB antennas [23], inverted F-antennas [24], and dual mode antennas [25]. The published data so far provides a trade-off between antenna gain, operational bandwidth, thickness of the antenna, dielectric constant of the substrate and specific absorption rate (SAR), and hence an optimum geometry design still is required in terms of isolation characteristics, biocompatibility, node placement location independency and flexibility issues. Due to poor conductivity and the lossy nature of human body tissues, the microwave power tends to propagate into the human body, resulting in considerable dissipative losses. Hence, SAR is also an important factor to optimize.

In this paper, printed monopole geometry is fabricated using ultra thin substrate with a high index dielectric constant, fed through an optimized micro-strip feed line structure. The near-field and far-field radiation characteristics are measured and an SAR analysis is presented for fat and bone tissues, for an energized power ranging from 0.5 to 3 W. Tri-banding is accomplished by introducing fractals with printed structure as a virtual combination of capacitance and inductance. This latter has been simulated and tested to understand the impact of transceiver bending on the antenna's radiation characteristics. The directivity characteristics and SAR calculations for bended fractal geometry simulated for power levels ranging from 100 to 800 mW. The simulated and measured results fit well and confirm uniform characteristics irrespective of the on-body location of transceiver.

Table 1 Rogers RO3010 substrate parameters

Substrate parameters	Values
Dielectric constant (ε_r)	10.2
Substrate thickness	250 µm
Copper thickness	27 µm
Thermal conductivity	0.66 W/K/m
Loss tangent (δ)	0.0023

Materials and methods

An effective transceiver helps in relaying diverse data types based from on-body sensors, in order to gather useful clinical data. The typical parameters recorded by medical professionals via wearable devices for body centric communication include; body temperature, heart rate, respiration rate, blood pressure, pulse oxygenation and glucose levels. Sensing locations for the captioned parameters using bio-signals are summarized in Table 1.

A direct communication pathway between the on-body chips and external circuitry is illustrated in Fig. 1.

As illustrated in Fig. 1 the data shared to external wireless base transceiver station (BTS) can be used by different care providers at different points of care. However, implementing wearable sensor technologies will require change in the delivery model, responsibility and data sharing between doctors, other care providers and even other organisations including informal carers such as families [26]. A key element of any successful solution will be a durable and efficient on-body antenna design. Such an antenna will be described in the next section.

Antenna geometry and design

The monopole antenna described in this paper was designed using ultra-thin and flexible Rogers RO3010 substrate with properties illustrated in Table 1 [27]. The antenna is polarized orthogonal to the body surface to achieve a strong diffracted pattern around the body surface is ensured.

The design of a trapezoidal monopole antenna involves the design of equilateral triangular patch with a base of the same width as the 50 Ω microstrip line energizer. The equilateral triangular patch has side length 'x', substrate thickness 'h' and relative dielectric constant (ε_r). The electric field $\boldsymbol{E}$ expression in terms of magnetic vector magnetic potential $\boldsymbol{A}$ and the magnetic field $\boldsymbol{H}$ in terms of electric vector potential $\boldsymbol{F}$ is given by Eqs. (1, 2):

$$\boldsymbol{E} = -j\omega\boldsymbol{A} + \frac{\nabla(\nabla \times \boldsymbol{A})}{j\omega\varepsilon\mu} \tag{1}$$

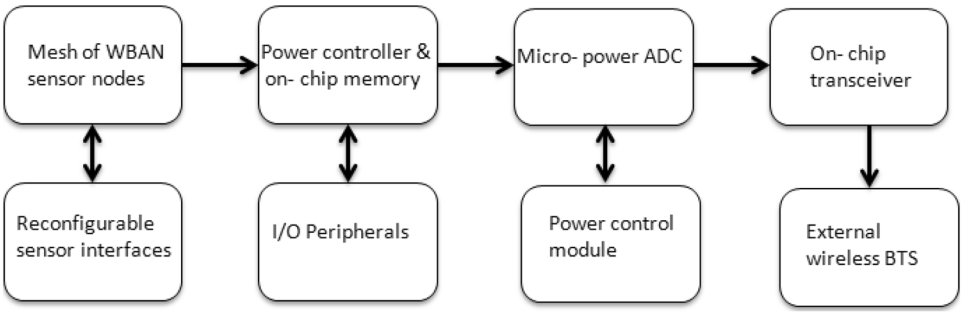

Fig. 1 A schematic exhibit of communication scheme between on-body and external sensor nodes

$$\boldsymbol{H} = -j\omega\boldsymbol{F} + \frac{\nabla(\nabla \times \boldsymbol{F})}{j\omega\varepsilon\mu} \tag{2}$$

In case of equilateral triangle monopole design involving both electric and magnetic potentials, a pair of couple equations for $\boldsymbol{E}$ and $\boldsymbol{H}$ follow;

$$\boldsymbol{E} = \frac{\nabla(\nabla \times \boldsymbol{A})}{j\omega\varepsilon\mu} - j\omega\boldsymbol{A} - \frac{1}{\varepsilon}(\nabla \times \boldsymbol{F}) \tag{3}$$

$$\boldsymbol{H} = \frac{\nabla(\nabla \times \boldsymbol{F})}{j\omega\varepsilon\mu} - j\omega\boldsymbol{F} + \frac{1}{\mu}(\nabla \times \boldsymbol{A}) \tag{4}$$

The resonant frequency f_r of ETMA for the dominant mode with side length x is given by Eqs. 5–6 [28].

$$f_r = \frac{2c}{3x\sqrt{\varepsilon_r}}\sqrt{m^2 + mn + n^2} \tag{5}$$

$$f_r = \frac{2c}{3x\sqrt{\varepsilon_r}} \tag{6}$$

In Eqs. (5, 6), ε_r was replaced with ε_{eff} and x with x_{eff} for a precised expression for resonant frequency and expressed by Eqs. (7–10) [29, 30];

$$\varepsilon_{eff} = \frac{1}{2}(\varepsilon_r + 1) + \frac{1}{4}\frac{(\varepsilon_r - 1)}{\sqrt{1 + (12h/x)}} \tag{7}$$

$$x_{eff} = x\frac{h}{\sqrt{\varepsilon_r}} \tag{8}$$

$$f_r = \frac{2c}{3x_{eff}\sqrt{\varepsilon_{eff}}} \tag{9}$$

Microstrip feed line and optimized design configuration

To energize the radiator, an optimum length of transmission line feed was found to be 243 µm using Eqs. (10, 11) for a 50 Ω transmission line (Rogers RO3010) substrate. The edge feed topology enabled tunable antenna impedance behavior and impedance is identical at both resonant ends.

$$\frac{W}{h} < 1; Z_o = \frac{60}{\sqrt{\varepsilon_{eff}}} \times \ln\left(\frac{8h}{W} + \frac{W}{4h}\right) \tag{10}$$

$$\frac{W}{h} \geq 1; \quad Z_o = \frac{120\pi}{\sqrt{\varepsilon_{eff}}} \times \frac{1}{(W/h) + 1.393 + 0.677 \times \ln((w/h) + 1.444)} \tag{11}$$

The schematic of the designed monopole antenna is exhibited in Fig. 2. The final substrate dimensions were $55.78 \times 45.3 \times 0.250$ mm^3 and other parametric values include; loss tangent (δ) of 0.0023, copper thickness of 27 µm and high dielectric constant (ε_r) of 10.2. Due to the ultra-thin nature of substrate and a higher value of dielectric constant, the impedance bandwidth of the radiator has significantly improved.

The width of the base of the trapezoidal element B_w is 243.86 µm and the distance from base of trapezoidal element to the top of element P_l is 15.01 mm. The length of feed line F_l was 30.31 mm and the width of feed line F_w was 243.86 µm. Similarly, the width of the top of the trapezoidal element T_w was 27.8894 mm and the length of the ground plane G_l is 30.20 mm.

Results

Return loss and directivity characteristics of the on-body transceiver

The fabricated antenna geometry is illustrated in Fig. 3a. The far field radiation patterns are presented in Fig. 3b. The radiation power from the evolved geometry has a gain of 2.69 dBi measured using a Rohde & Schwarz ZVA series ZVA50 Vector Network Analyzer (VNA) and the results are presented in Fig. 3c. Figure 3c reveals a good agreement between the simulated and measured results for the reflection coefficient (S_{11}) plotted against the operational frequency. The simulated return loss using CST® of the designed radiator was 17 dB at 2.4 GHz, with a − 10 dB bandwidth of 380 MHz (15.83%). FEKO® simulated the return loss of the antenna as 14.5 dB, with a − 10 dB bandwidth of 620 MHz

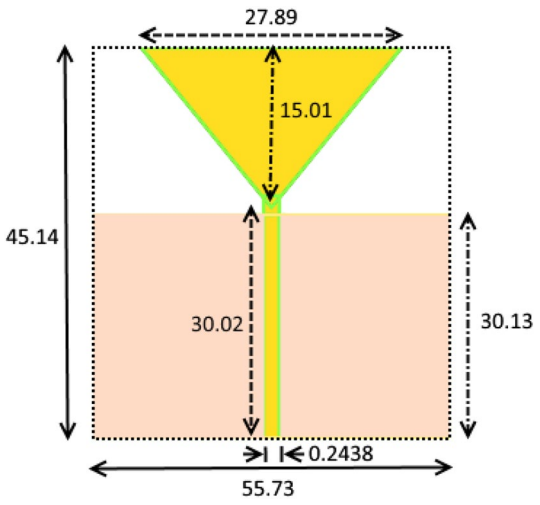

Fig. 2 A schematic view of ultra-thin flexible monopole antenna

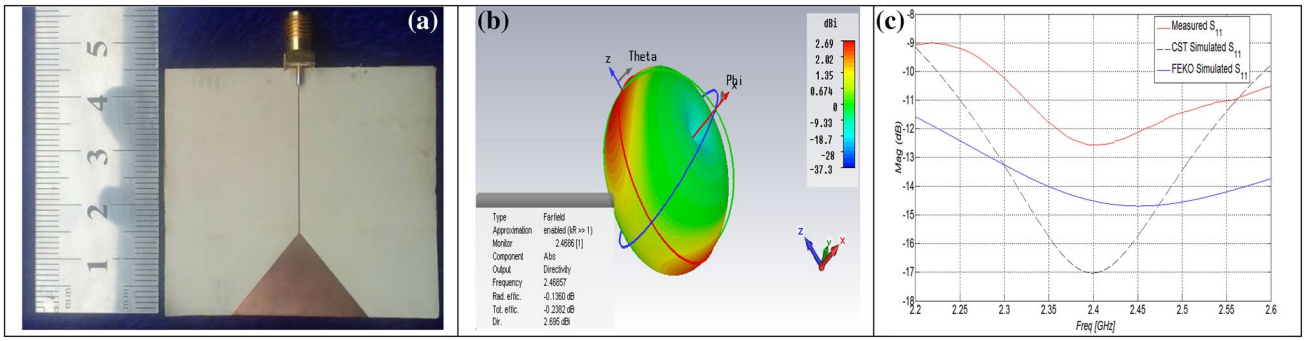

Fig. 3 An illustration of fabricated transceiver geometry, radiation pattern and experimental verification. **a** An exhibit of fabricated monopole antenna. **b** 3D radiation patterns for the simulated antenna geometry at 2.4 GHz. **c** Measured and simulated reflection coefficient S_{11} for printed monopole antenna

Table 2 Tissues characteristics of FAT and bones

Tissues	FAT	Bones
Relative permittivity	5.28	11.38
Conductivity	0.10	0.39
Mass density	1100	1850
Thermal Cond.	0.20	0.41
Heat Cap.	2.50	1.30
Blood flow	1700	3400
Metabolic rate	300	610

(25.83%). The experimentally confirmed return loss was 12.67 dB, with a − 10 dB bandwidth of 340 MHz (13.75%). Tables 3 and 4 reveal that the values of local SAR are much higher as compared to the average SAR.

The near field profile computed for an average thickness of clothing and positioned at 6–7 mm from human body. For SAR calculations, human arm was modeled in 3D with parameters illustrated in Table 2.

The simulations performed for an input power of 1 W and associated average SAR values for fat tissues, bone tissues were computed, and results are presented in Fig. 4.

Figure 4 illustrates that fat tissues experience relatively steep increase in temperature than the bone tissues for an input power level of 1 W and corresponding SAR of 0.59 as compared to bone tissues with energizing power of 3 W and SAR of 0.739. The computed SAR parameters for different excitation powers are illustrated in Tables 3 and 4.

Figure 5 illustrates that fat tissues experience relatively steep increase in SAR compared to bone tissue for input power level between 0.5 and 3 W.

The resonant frequencies of the monopole were determined using Eq. 12.

$$f_{nr} = k\frac{c}{h}\cos\left(\frac{\gamma}{2}\right)\delta^{nr} \tag{12}$$

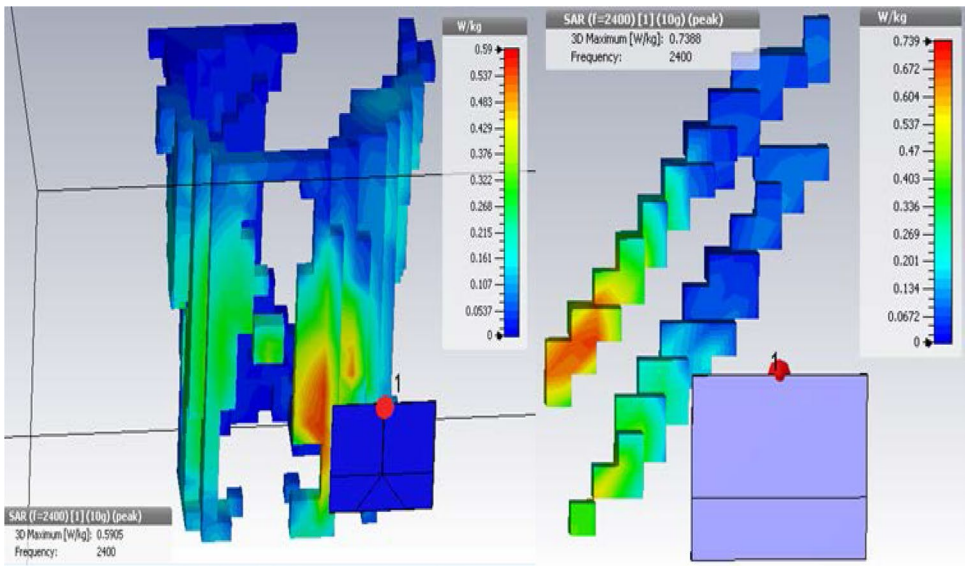

Fig. 4 SAR distribution of antenna for fat tissues and bone tissues

Table 3 SAR values against energised power for FAT tissues

P [W]	Local SAR [W/kg]	Max. SAR (1 g) [W/kg]	Max. SAR (10 g) [W/kg]	Calc. (1 g) [s]	Calc. (10 g) [s]
0.5	0.97	0.39	0.29	10	139
1	1.94	0.79	0.59	9	150
1.5	2.91	1.18	0.89	11	153
2	3.88	1.58	1.18	9	140
2.5	4.85	1.98	1.48	10	145
3	5.82	2.38	1.77	8	147

Table 4 SAR values against energized power of Bone tissues

P [W]	Local SAR [W/kg]	Max. SAR (1 g) [W/kg]	Max. SAR (10 g) [W/kg]	Calc. (1 g) [s]	Calc. (10 g) [s]
0.5	1.18	0.21	0.12	5	78
1	2.36	0.42	0.25	5	90
1.5	3.54	0.62	0.37	4	87
2	4.72	0.83	0.49	4	86
2.5	5.91	1.04	0.62	5	85
3	7.09	1.25	0.74	4	88

In Eq. 12, f_{nr} resonant frequency of n band numbers, c represents the speed of light, γ is the flare angle, δ is the similarity factor, h is the height of monopole, k is a constant and is a function of substrate type and thickness.

The return loss plots due to discontinuity mismatch with the terminating load against frequency are exhibited in Fig. 6.

The effects of bending on transceiver's S-parameter characteristics due to on-body movement are presented in Fig. 7.

The self-similar fractals improve the radiation characteristics of the designed transceiver, as illustrated in Fig. 7. The directivity achieved was 6.07 dBi, 7.57 dBi and 7.57 dBi for foot, head and arm regions sensor nodes respectively and is elaborated in Fig. 8. The directivity of the geometry was 6.07 dBi, 7.57 dBi and 7.57 dBi for foot, head and arm regions sensor nodes respectively.

Assessment of SAR attributes and impact of lateral misalignment

In order to determine the SAR characteristics, phantom model of foot, head and arm is designed in CST MWS. Human body tissues are highly conductive and dielectric in nature. If a wearable antenna is placed in close proximity to the human body, some of the available power is reflected backwards and absorbed within human body tissues resulting in higher values of SAR. SAR values range from (10 g) W/kg = 0.0988–0.790 for foot, head SAR values ranges from (10 g) W/kg = 0.0987–1.569 and (10 g) W/kg = 0.258–2.061 for human arm as confirmed in Fig. 9.

The effect of lateral misalignment on wearable transceiver performance is presented in Fig. 10 and the impact on return loss characteristics by positioning transceivers on different body locations is exhibited in Fig. 11.

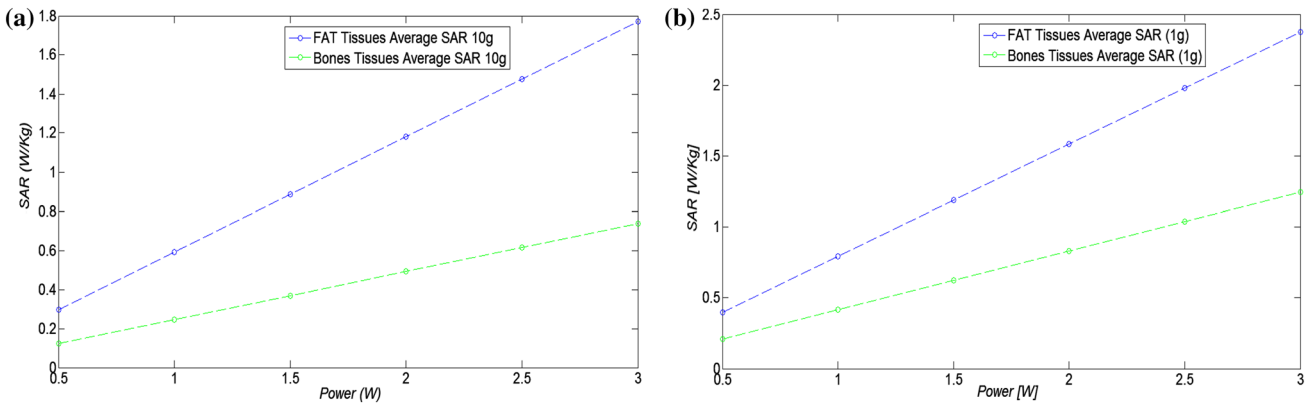

Fig. 5 Plots of energized power against average SAR (10 g) levels for fat and bone tissues. **a** Input power against average SAR (10 g) levels for fat and bone tissues. **b** Input power against average SAR (1 g) levels for fat and bone tissues

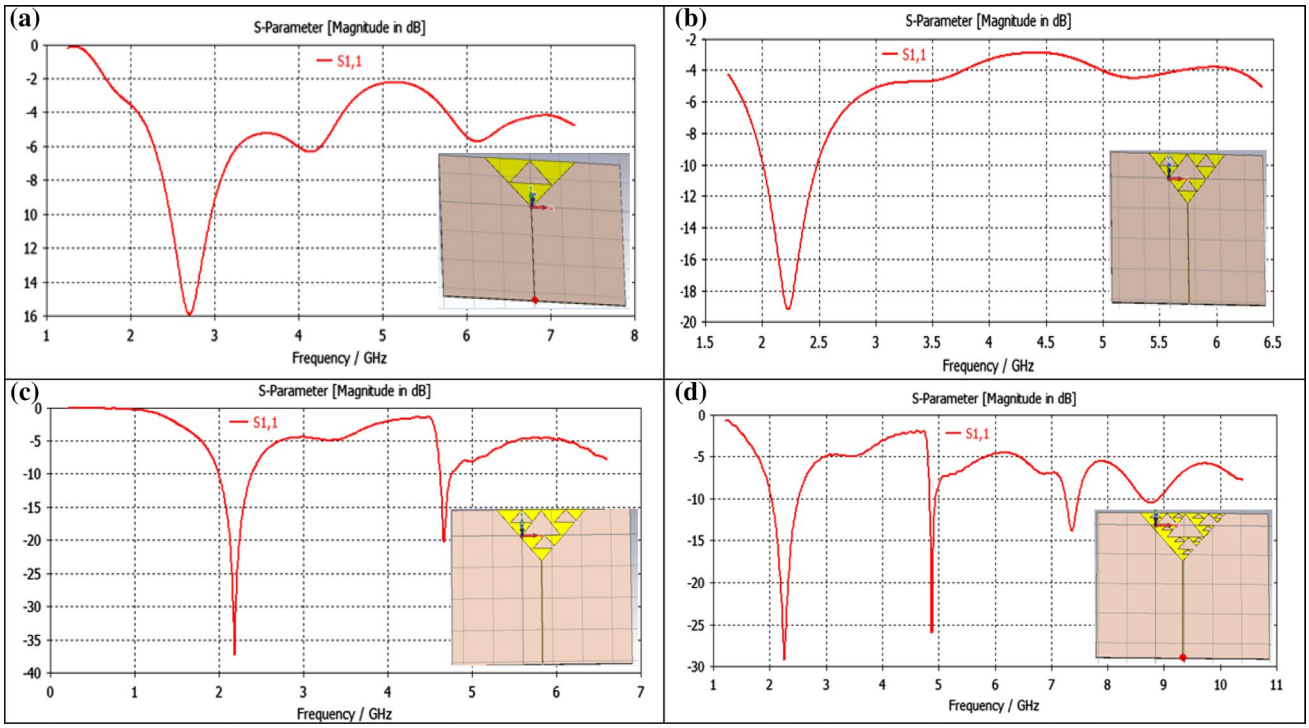

Fig. 6 Return loss against frequency for uni-band, dual band and tri-band transceiver geometry. **a** First iteration of fractal based transceiver structure. **b** Second iteration of fractal based transceiver structure. **c** Second iteration of shifted fractal based structure. **d** Third iteration of fractal based structure

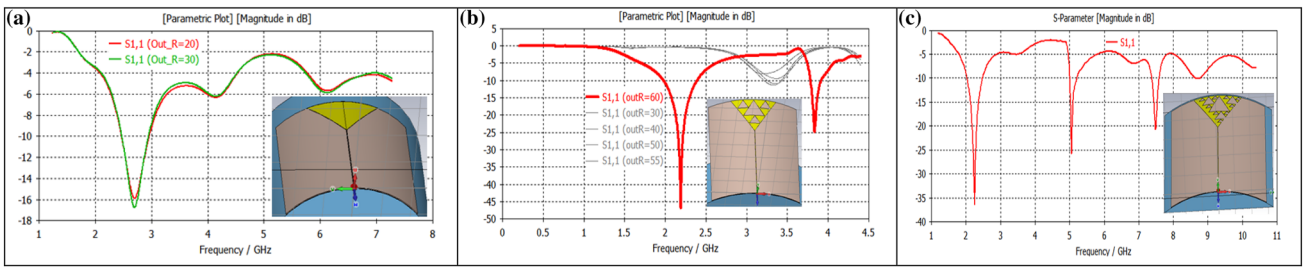

Fig. 7 Effects of bent on return loss for uni-band, dual band, and tri-band configurations. **a** Single band 20° bent antenna. **b** Dual band 20° bent antenna. **c** Tri-bent 20° bend antenna

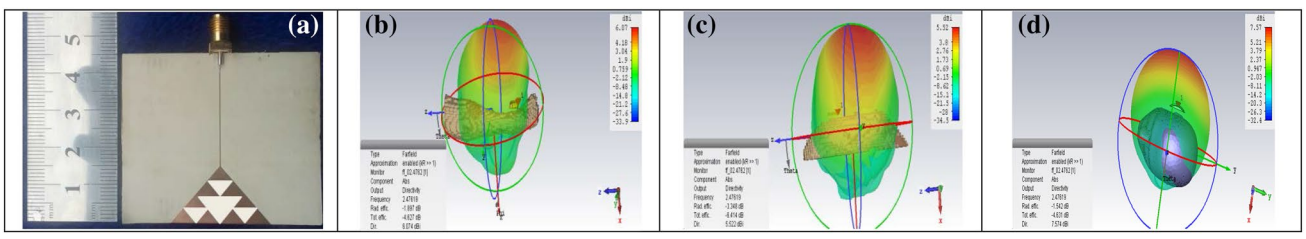

Fig. 8 Evolved dual band transceiver geometry and the gain characteristics at multiple body positions. **a** Fabricated dual band transceiver geometry. **b** 3-D gain pattern of 20° bent dual antenna placed at foot. **c** 3-D gain pattern of 20° bent dual antenna placed at head. **d** 3-D gain pattern of 20° bent dual antenna placed at arm

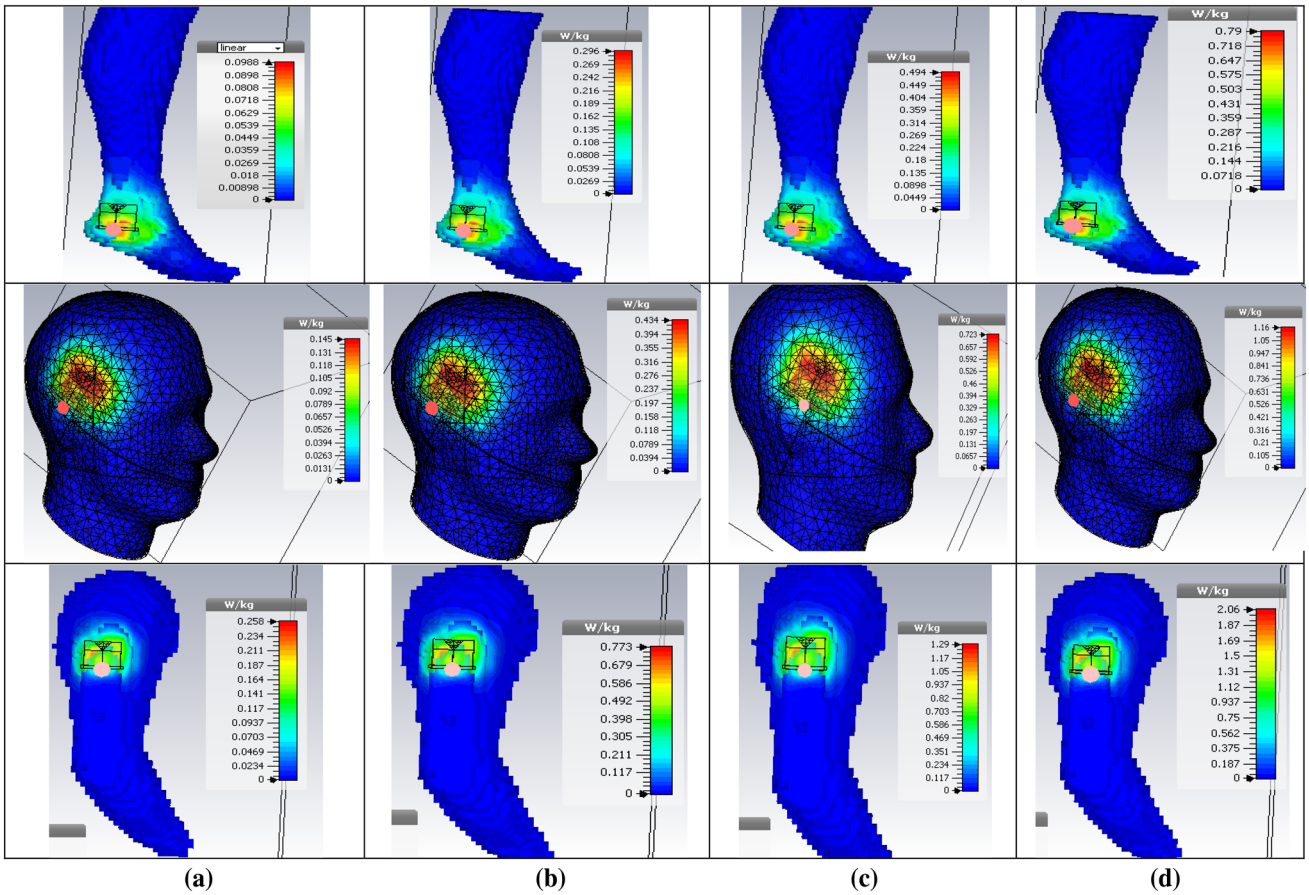

Fig. 9 SAR characteristics for foot, arm and head for energized power levels ranging from 100 to 800 mW. Column **a** SAR calculations for 100 mW. Column **b** SAR calculations for 300 mW. Column **c** SAR calculations for 500 mW. Column **d** SAR calculations for 800 mW

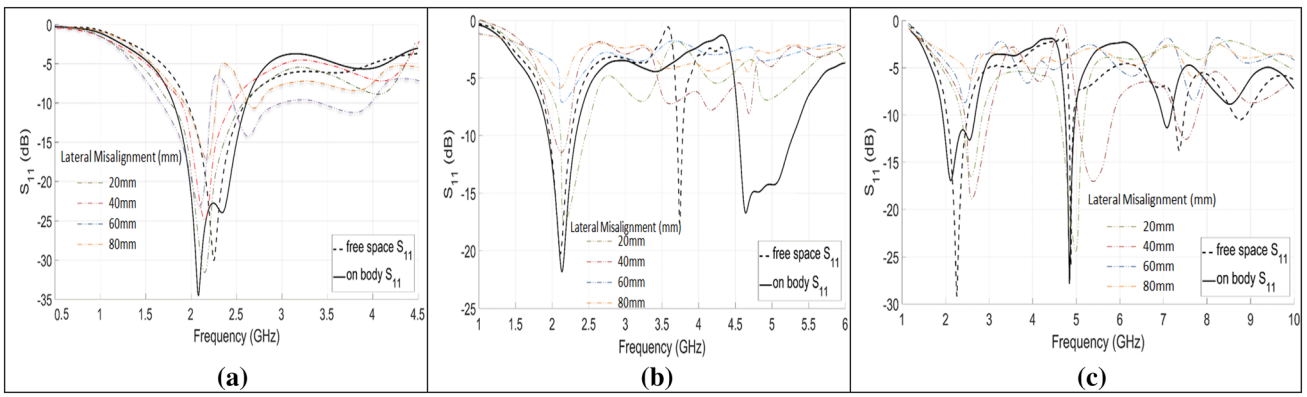

Fig. 10 Effects of lateral misalignment on return loss for uni-band, dual band, and tri-band configurations. **a** Single band on body antenna. **b** Dual band on body antenna. **c** Tri-band on body antenna

Monitoring of real time data with sensing modules and cloud fusion

Two accelerometers were used to capture live data emanating from axial directions. The captured data is illustrated in Fig. 12. The data from 15 feet wearable transceivers were simultaneously recorded and the waveforms are presented in Fig. 13 in both un-synchronized and synchronized modes.

The aim was to validate collected data and to process data streams from on-body sensors. Kalman filtering routine

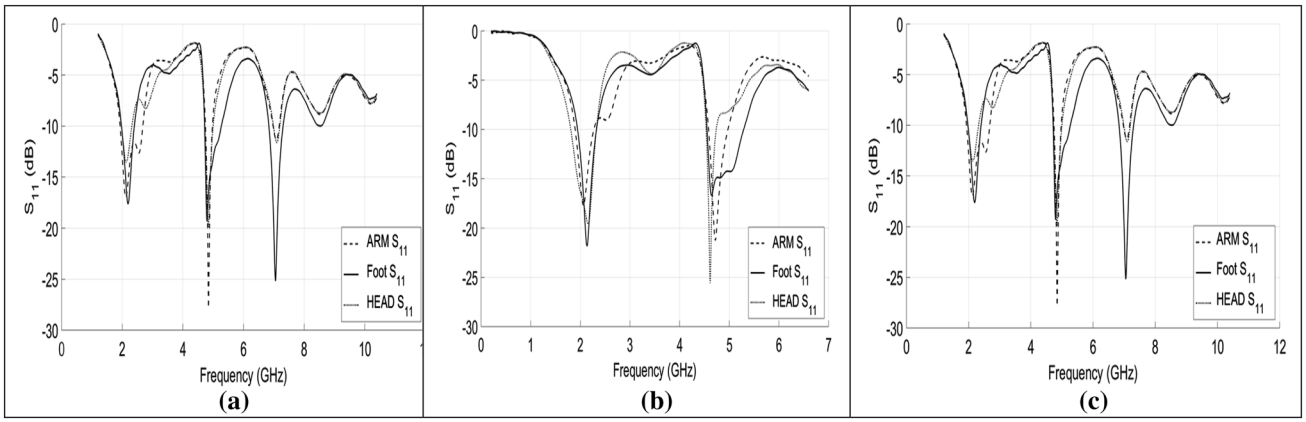

Fig. 11 The effect on return loss characteristics against frequency for different body locations **a** first iteration fractals for the developed antenna geometry, **b** second iteration fractals for the developed antenna geometry, **c** third iteration fractals for the developed antenna geometry

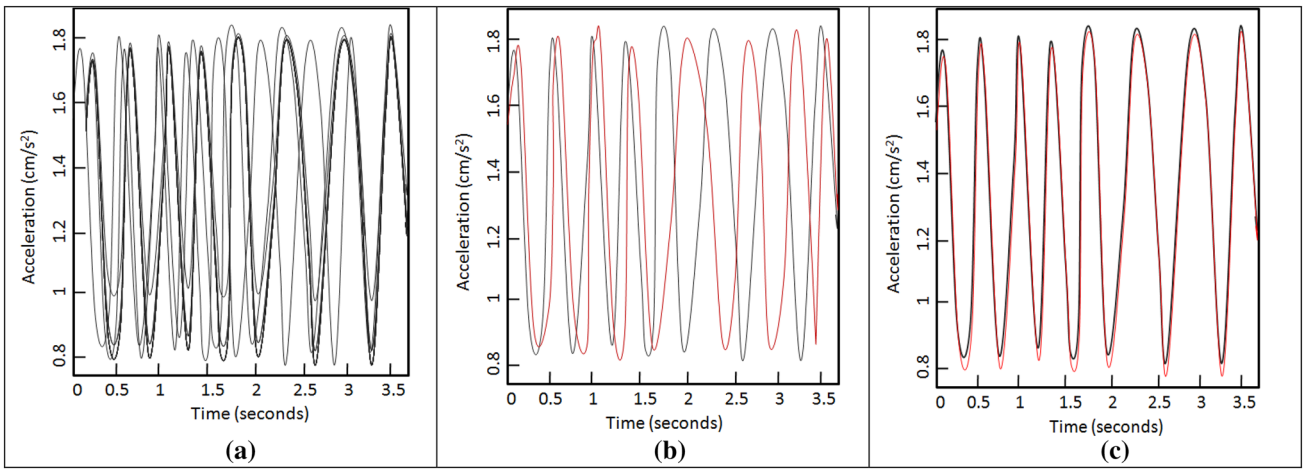

Fig. 12 Real time data acquisition from on-body transceivers. **a** Signals from multiple on-body transceivers. **b** Signals from the transceivers placed on foot and arm locations in un-synchronized mode. **c** Signals from transceivers placed on foot and arm locations in synchronized mode of operation

enabled large-scale data sharing and collaborations among the users and the cloud. The routine is illustrated in Fig. 14.

Discussion

A schematic of finite difference time domain (FDTD) recursive routine is presented in Fig. 15.

Figure 7 confirms that not even a trivial shift in the frequency and return loss characteristics was observed. Multiband non-planar antennas are considered compatible but have narrower bandwidth at lower frequency bands. Sufficient bandwidths require a considerable thickness that makes them difficult to employ in wearable technologies. Therefore, the concept of Sierpinski gasket fractals was used to implement ultra-thin multiband transceiver log-periodically spaced by a factor of two. The repeated pattern of similar fractals permitted miniaturization and broadband characteristics. The desired resonant frequency and geometrical properties of fractal radiators after imposing associated boundary conditions provide similarity factor for optimized SAR characteristics.

The proposed geometry achieves high-directivity due to more active regions offered by fractals. The presence of fractals initiates additional active regions around the geometry vicinity and that resulted in increased directivity. The proposed antenna has better operational characteristics and reduced antennas size as compared to the already reported results as illustrated in Table 5.

Since communication is restricted to the proximity of the body, the lateral misalignment of sensor nodes leads to first side lobe of the radiation pattern coupled to main

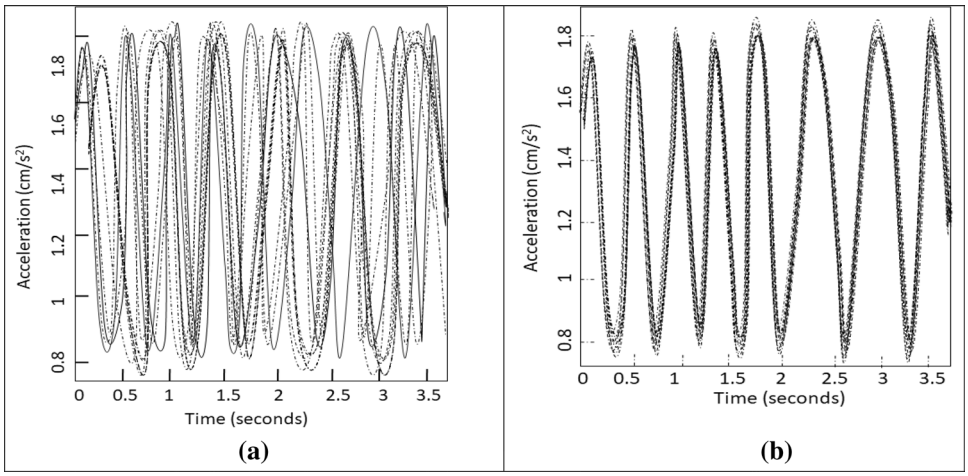

Fig. 13 **a** Real time data acquisition from 15 users having on-body foot transceivers in an un-synchronized mode. **b** Signals from 15 users having wearable foot transceivers in synchronized mode of operation

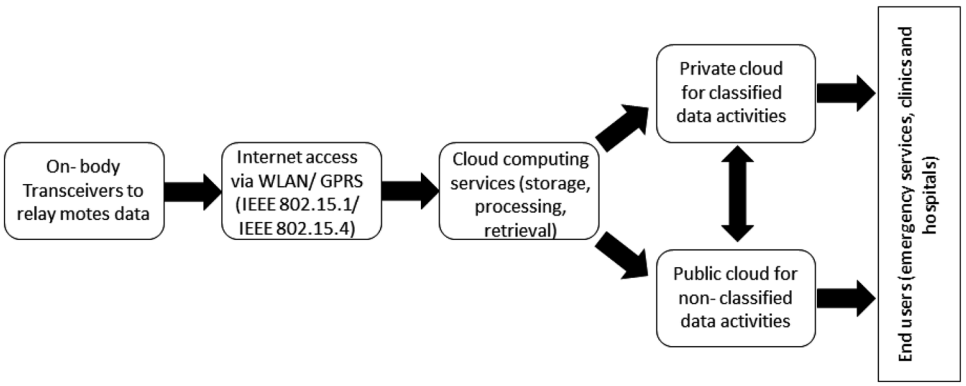

Fig. 14 A sequential flow scheme of the activities for establishing end–end connectivity

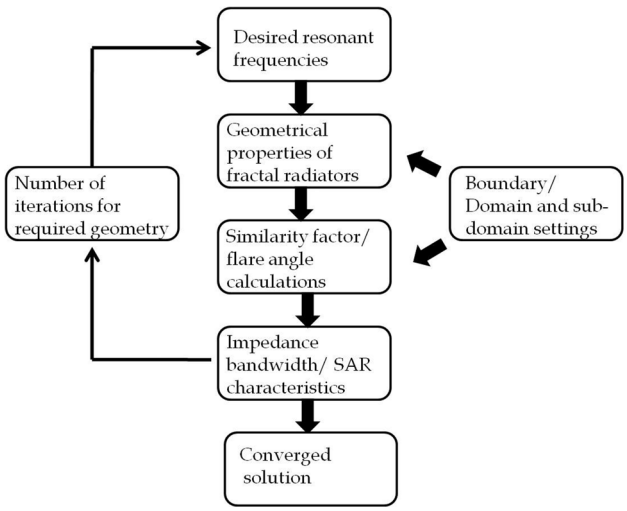

Fig. 15 An illustration of sequential steps involved in determining optimized bandwidth/SAR characteristics

beam readings. This is particularly challenging, as the signal level at the center of the first lobe is greater than the signal level at the edges of the main beam resulting in counterfeit impression of the main beam profile. The impact of lateral misalignment was included and optimized through tuning in the preceding section. Each sensor has a different set of attributes for depicting the readings with regard to the position of on-body sensors.

Figure 13a presents the human activity motion signals acquired through multiple on-body transceivers. For the sake of comparison, the signals from foot and arm sensors without data synchronization are exhibited in Fig. 13b. The time deviation factor was 85 ms in this case. Figure 12c is an illustration of the same data as in Fig. 13b but with data synchronized. The continued operation of transceivers for wearable health informatics over 48 h with data synchronized and error was found less than 4 ms. Mobile computing and virtual machine (VM) based cloud computing architecture has been used for client/server, collaborative and broadcast activities. A schematic illustrating the sequential flow of end–end connectivity presented in Fig. 15.

Conclusions

A novel ultra-thin multiband on-body transceiver geometry is designed, optimized and fabricated for multifarious health informatics applications. Microwave characteristics of the

Table 5 A comprehensive performance comparison of the proposed geometry with the existing literature

References	Dimensions (mm^3)	Gain/directivity/BW %	Detuning %	SAR (W/kg)/ distance from body
[31]	$100 \times 100 \times 6$	2.42/9.85	NA	0.072/15
[32]	$100 \times 100 \times 4.5$	2.5/NA	NA	0.046/10
[33]	$65.7 \times 65.7 \times 1.5$	4.3/18	2.5%	0.638/NA
Proposed	$45.14 \times 55.73 \times 0.254$	2.69/13.75	1.7%	0.0988/2

evolved geometry is presented for on-body communication. The simulated return loss using CST® of the designed radiator was − 17 dB at 2.4 GHz, with − 10 dB bandwidth of 380 MHz (15.83%). FEKO® simulated return loss of the transceiver was found to be 14.5 dB with − 10 dB bandwidth of 620 MHz (25.83%). The experimentally confirmed return loss is very promising with 12.67 dB return loss and − 10 dB bandwidth of 340 MHz (13.75%). The results suggest that a trade-off existed between the antenna thickness and impedance bandwidth. Human body fatty tissues exhibited a higher absorption coefficient as compared to bone tissues for a specific energized level. As expected, the results reveal a ramp function relationship between excitation power levels and average SAR values. Multi-banding using fractals resulted in tri-band communication channels within ultra wide band (UWB). Similarly, the flexibility of the evolved transceiver configuration allows more freedom in terms of body maneuvering. Real time measurements to acquire live data over a period of 2 days confirmed the efficacy of evolved transceiver. The directivity and SAR characteristics confirm an efficient coupling to the external wireless technologies. Furthermore, the concept is validated for 15 different users through real time data acquisition, relaying and processing.

Acknowledgements Dr. Engr. Junaid Zafar acknowledges the grant entitled "Pakistan Programme for Collaborative Research", an initiative of Higher Education Commission, Pakistan. Haroon Zafar is supported by an Irish Research Council (IRC) "Enterprise Partnership Scheme" Postdoctoral Research Fellowship (EPSPD/2016/20) and New Foundations Grant 2016.

Compliance with ethical standards

Conflict of interest All the authors have no conflict of interest.

Ethical approval This article does not contain any studies with human participants or animals performed by any of the authors.

References

1. Amjadi M, Kyung K, Park I (2016) Stretchable, skin-mountable, and wearable strain sensors and their potential applications. Adv Funct Mater 26(11):1678–1698
2. Khan Y, Ostfeld AE, Lochner CM et al (2016) Monitoring of vital signs with flexible and wearable medical devices. Adv Mater 28(22):4373–4395
3. Zhang YT, Zheng YL, Lin WH (2013) Challenges and opportunities in cardiovascular health informatics. IEEE Trans Biomed Health Inform 30(3):633–642
4. Peltokangas M, Telembeci AA, Verho J (2017) Parameters extracted from arterial pulse waves as markers of atherosclerotic changes: performance and repeatability. IEEE J Biomed Health Inform. https://doi.org/10.1109/JBHI.2017.2679904
5. Bonato P (2010) Wearable sensors and systems. From enabling technology to clinical applications. IEEE Eng Med Biol Mag 29:25–36
6. Cao H, Leung V, Cho C (2009) Enabling technologies for wireless body area networks: a survey and outlook. IEEE Commun Mag 47(12):84–93
7. Servati A, Zou L, Wang ZJ et al (2017) Novel flexible wearable sensor materials and signal processing for vital sign and human activity monitoring. Sensors 17(7):1622–1628
8. Takei K, Honda W, Harada S et al (2015) Toward flexible and wearable human-interactive health-monitoring devices. Adv Healthc Mater 4(4):487–500
9. Kim J, Salvatore GA, Araki H, Battery-free, stretchable optoelectronic systems for wireless optical characterization of the skin. Sci Adv 2(8):1546–1556
10. Wang L, Yang G, Huang J (2010) A wireless biomedical signal interface system on-chip for body sensor networks. IEEE Trans Biomed Circuits Syst 4(2):112–117
11. Kim DH, Ghaffari R, Rogers JA (2012) Flexible and stretchable electronics for bio-integrated devices. Annu Rev Biomed Eng 14:113–128
12. Ibarra E, Antonopoulous A, Kartsakli E (2016) QoS-aware energy management in body sensor nodes powered by human energy harvesting. IEEE Sens J 16(2):542–549
13. Yi C, Alfa AS, Cai J et al (2016) An incentive-compatible mechanism for transmission scheduling for delay sensitive medical packets in e-health networks. IEEE Trans Mob Comput 15(10):2424–2436
14. Chen M, Qian Y, Chen J et al (2016) Privacy protection and intrusion avoidance for cloudlet base medical data sharing. IEEE Trans Cloud Comput 9:1–13
15. Li M, Lou W, Ren K et al (2010) Data security and privacy in wireless body area networks. IEEE Wirel Commun 17(1):51–58
16. Kaur G, Kaur A, Dhaliwal B BS (2015) Antennas for bio-medical applications. Biomed Eng Lett 5(3):203–212
17. Scarpello ML, Kurup D, Rogier H et al (2011) Design of an implantable slot dipole conformal flexible antenna for biomedical applications. IEEE Trans Antennas Propag 59(10):3556–3564
18. Liu C, Guo YX, Xiou S et al (2014) Capacitively loaded circularly polarized implantable patch antenna for ISM band biomedical applications. IEEE Trans Antennas Propag 65(2):2407–2417
19. Reig C, Navarro EA (2014) Printed antennas for sensor applications: a review. IEEE Sens J 14(8):2406–2418

20. Tahir FA, Javed A (2015) A compact dual band frequency reconfigurable textile antenna for wearable applications. Microw Opt Technol Lett 57(10):2251–2257
21. Liu Z, Guo Y (2014) Compact low-profile dual band meta-material antenna for body centric communications. IEEE Antennas Wirel Propag Lett 14:863–866
22. Singh N, Singh AK, Singh VK (2015) Design and performance of wearable ultra wideband textile antennas for medical applications. Microw Opt Technol Lett 57(7):1553–1557
23. Aun NF, Soh PJ, Al-Hadi AA et al (2017) Revolutionizing wearables for 5 G technologies: recent developments and future perspective for wearable devices and antennas. IEEE Microw Mag 18(3):108–124
24. Lin C, Saito K, Takahasha M (2012) A compact planar inverted F-antenna for 2.45 GHz on body communications. IEEE Trans Antennas Propag 60(9):4422–4426
25. Soh PJ, Bergh B, Xu H et al (2013) A smart wearable textile array system for biomedical telemetry applications. IEEE Trans Microw Theory Tech 61(5):2253–2261
26. Lewy H (2015) Wearable technologies-future challenges for implementation in health care services. Healthc Technol Lett 2(1):2–5
27. http://www.rogerscorp.com/acs/products/39/RO3006-and-RO3010-Laminates.aspx. Accessed 25 Sept 2017
28. Ojaroudi M (2009) Printed monopole antenna with a novel band-notched folded trapezoid for ultra wideband applications. J Electromagn Waves Appl 23:2513–2522
29. Wu XH, Kishk (2008) A study of an ultra-band omni-directional rolled antenna with trapezoidal cuts. IEEE Trans Antennas Propag 56(1):259–263
30. Liu J, Zhong S, Esselle KP (2011) A printed elliptical monopole antenna with modified feeding structure for bandwidth antenna. IEEE Trans Antenna Propag 59(2):667–670
31. Lago H, Soh PJ, Jamlos MF, Shohaimi N, Yan S, Vandenbosch GAE (2016) Textile antenna integrated with compact AMC and parasitic elements for WLAN/WBAN applications. Appl Phys A 122(12):1059–1062
32. Yan S, Soh PJ, Vandenbosch GAE (2014) Low-profile dual-band textile antenna with artificial magnetic conductor plane. IEEE Trans Antennas Propag 61(12):6487–6490
33. Raad HR, Abbosh AI, Al-Rizzo HM, Rucker DG (2013) Flexible and compact AMC based antenna for telemedicine applications. IEEE Trans Antennas Propag 61(2):524–531